Il presente lavoro è stato pubblicato su Carbohydrate Polymers 163(2017) 280–291 con doi: https://dx.doi.org/10.1016/j.carbpol.2017.01.064

Insight Into Halloysite Nanotubes-Loaded Gellan Gum Hydrogels For Soft Tissue Engineering Applications

Maria A. Bonifacio,[1†] Piergiorgio Gentile,[2†] Ana M. Ferreira,[2] Stefania Cometa,[3] Elvira De Giglio [1*]

[1*]Dept. of Chemistry, University of Bari Aldo Moro, Via E. Orabona 4, Bari, 70126, Italy.

maria.bonifacio@uniba.it;

[2] School of Mechanical and Systems Engineering, Newcastle University, Stephenson Building, Claremont Road, Newcastle upon Tyne, NE1 7RU, UK.

piergiorgio.gentile@newcastle.ac.uk; ana.ferreira-duarte@newcastle.ac.uk

[3]Jaber Innovation s.r.l., via Calcutta 8, Rome, 00144, Italy.

stefania.cometa@virgilio.it

[†] *These authors equally contributed to the work.*

* Corresponding author. Tel/Fax: +39 080 5442021.

E-mail address: elvira.degiglio@uniba.it (E. De Giglio)

Abstract

A tri-component hydrogel, based on gellan gum (GG), glycerol (Gly) and halloysite nanotubes (HNT), is proposed in this work for soft tissue engineering applications. The FDA-approved GG polysaccharide has been recently exploited as biomaterial because its biomimetic features. Gly is added as molecular spacer to improve hydrogel viscosity and mechanical properties. HNT incorporation within the hydrogel offers the versatility to improve the GG-Gly biocompatibility with potential incorporation of target biomolecules. In this work, hydrogels with different composition ratios are physically crosslinked for tuning physico-mechanical properties. An accurate physico-chemical characterization is reported. HNT addition leads to a water uptake decrease of 30-35% and tuneable mechanical properties with a compressive Young's modulus ranging between 20 and 75kPa. Finally, *in vitro* study with human fibroblasts on GG-Gly hydrogels loaded with 25% HNT offered the higher metabolic activities and cell survival up to 7 days of incubation.

Keywords: Gellan gum, Halloysite nanotubes (HNT), Hydrogel, Human fibroblasts, Tissue engineering**.**

Chemical compounds studied in this article

Gellan gum (PubChem SID: 135330201); Halloysite nanotubes (PubChem CID: 121233131); Glycerol (PubChem CID: 753); Calcium Chloride (PubChem CID: 5284359).

1. Introduction

In the last years, the role of biomaterials in tissue engineering has gone beyond the classic view of passive support for cell growth: the knowledge of the wide array of cell-matrix interactions has led to a more conscious selection of biomaterials that mimic the complex spatio-temporal cues of extracellular matrix (Chen & Liu, 2016). Hydrogels represent an interesting class of materials, with high water content, tunable properties and ease to be processed under physiological conditions (Annabi et al., 2014; De Giglio et al., 2011). In this scenario, biopolymer-based hydrogels stand out for biocompatible features, given by the remarkable similarity with extracellular matrix (Van Vlierberghe et al., 2011). Polysaccharides (e.g. gellan gum, alginate and chitosan) have the further advantage of releasing non-toxic monomers during degradation and, for this reason, are the most investigated biopolymers for biomedical applications (Pasqui et al., 2012). Gellan gum is an exopolysaccharide secreted by bacteria belonging to the Sphingomonas genus. Firstly isolated in 1979, gellan gum is currently manufactured *in vitro* by a straightforward fermentation process, avoiding batch-to-batch availability often associated to biopolymers (Prajapati et al., 2013). It consists of a linear chain of repeated tetrasaccharide units (L-rhamnose, D-glucose and D-glucuronic acid), commercially available under different trade names (e.g. Phytagel™, Gelrite®, Kelcogel®). In presence of cations, gellan gum undergoes a temperature-dependent gelation, forming stable hydrogels (Smith et al., 2007). After FDA approval as a food additive, this polysaccharide is widely exploited in food industry as thickening agent or emulsion stabilizer (Giavasis et al., 2000). Moreover, the potential of gellan gum is being studied in order to obtain new pharmaceutical formulations for oral, nasal and ophthalmic drug delivery (Osmałek et al., 2014; Wang et al., 2008).

Furthermore, thanks to its versatility, gellan gum is attracting increasing interest in the biomedical field and is being proposed for tissue engineering and regenerative medicine applications (Coutinho et al., 2010; Santhanam et al., 2016). A pioneering study by Shoichet et al. exploited a gellan gum matrix to support the adhesion and proliferation of neural stem cells, showing that the peptide-

modified gellan gum, together with the olfactory ensheathing glia, enhanced neural stem/progenitor cell survival (Silva et al., 2012). Cell adhesion improvement was also the focus of other works,(da Silva et al., 2014; Cerqueira et al., 2014) in which spongy-like gellan gum hydrogels were proposed as off-the-shelf 3D structures able to mimic the physico-chemical properties of ECM. Further application proposed recently by Mano and coworkers is the use of gellan gum as an injectable biomaterial (in form of blend with type I collagen), for bone regeneration purposes (Oliveira et al., 2016). The proposed biomaterial induced the differentiation of human adipose stem cells through a mechanotransduction pathway, without any medium supplement. Furthermore, one of the most promising strategies involving gellan gum provides the opportunity to develop composite materials adding inorganic particles (e.g. bioglasses) to the polymeric matrix (Gorodzha et al., 2016). With low filler loadings, the polymers mechanical features improve, as well as their bioactivity (Dawson & Oreffo, 2013). Among the inorganic particles available, natural nanoclay minerals provide the double advantage to be cost-effective and biocompatible (Lopes et al., 2014). Therefore, the aim of this work was to propose an innovative composite biomaterial in order to: (1) obtain a composite material with tunable physical and mechanical properties, and (2) evaluate its biological potential for tissue engineering applications. Specifically, in this work, halloysite nanotubes (HNT) have been proposed as inorganic fillers of gellan-based hydrogels. HNT are tubular aluminosilicate clays with a unique combination of features which are finding applications in numerous fields (Du et al., 2010). Beyond the broad availability, HNT are biocompatible and exhibit excellent mechanical properties (Yuan et al., 2015; Bottino et al., 2015; Liu et al., 2012). Several studies have reported the long-term stability and non-toxicity of HNT (White et al., 2012; Kamble et al., 2012). Being naturally dispersed, they do not require exfoliation procedures essential to obtain nanolayers from glass fibers or montmorillonite (Chalasani et al., 2013). Moreover, HNT mesoporous lumen could entrap bioactive molecules and subsequently release them, opening new frontiers in sustained drug delivery (Du et al., 2010). On the other hand, the hydroxyl groups distribution on the HNT outer

and inner surfaces allow a finely adjustable reactivity, achieved by targeted functionalisation (Zhang et al., 2016).

Some works on HNT composites with various polymers have been recently reported. As example, Liu and coworkers prepared alginate-HNT composite sponges by freeze-drying method resulting in increased scaffold stability and better fibroblast attachment (Liu et al., 2015). Similarly, chitosan and HNT formed a nanocomposite with significant thermal and mechanical improvements compared with the pure polymer (Liu et al., 2013). More recently, Fakhrullin et al. doped with HNT a chitosan–agarose–gelatin matrix and proposed it as advanced biomaterial for tissue engineering and sustained nanotube drug delivery (Naumenko et al., 2016). However, to the best of our knowledge, a nanoclay-polymer composite based on HNT and gellan gum has never been developed and investigated. This work aims at filling this gap, shedding light into the potential and intriguing applications of this new GG-based composite in soft tissue engineering. In this study, the preparation and characterization of hydrogels physically crosslinked with Ca^{2+} cations is reported. The hydrogels have been prepared varying the concentrations of HNT and glycerol, used as molecular spacer. Indeed, glycerol is commonly exploited as a biocompatible structural ameliorant to improve the physical and mechanical properties (Zhao et al., 2014). The composite hydrogels were characterized by morphological, physico-chemical and mechanical analyses. Ultimately, human fibroblasts were seeded on the surface and encapsulated into the hydrogel in order to test the potential applications as substrate or injectable biomaterial.

2. Materials and methods

2.1 Materials

Gellan gum (Phytagel™, formula weight 1,000 kg/mol; low acylation degree), hereafter coded as GG, halloysite nanoclay (HNT) and free flowing calcium chloride- Redi-dri™ ($CaCl_2$) were all supplied by Sigma-Aldrich (Italy). Glycerol (Gly) was provided by Baker Chemicals, Holland. The

ultrapure water employed throughout the experiments was obtained with a Milli-Q® Integral system equipped with a BioPak® ultrafiltration cartridge (Millipore, Merck).

2.2 Sample preparation

An aqueous solution of Gly (2 or 6% w/v) was heated at 90 °C and GG powder (2% w/v) added under vigorous stirring. To obtain the composite material, the dissolution step was followed by mixing with an aqueous suspension of HNT (final concentration 0, 0.2, 0.5 or 1% w/v), previously sonicated in cold water for 15 min. The codes and nominal compositions of the hydrogels are reported in Table 1.

Table 1. Nomenclature and nominal composition of the prepared hydrogels. All the % w/v are expressed in respect to the water.

Sample Code	GG content [%w/v]	Gly content [%w/v]	$CaCl_2$ content [%w/v]	HNT content [%w/v]
GG	2	--	0.025	--
GG-Gly(1:1)	2	2	0.025	--
GG-Gly(1:1)HNT10	2	2	0.025	0.2
GG-Gly(1:1)HNT25	2	2	0.025	0.5
GG-Gly(1:1)HNT50	2	2	0.025	1
GG-Gly(1:3)	2	6	0.025	--
GG-Gly(1:3)HNT10	2	6	0.025	0.2
GG-Gly(1:3)HNT25	2	6	0.025	0.5
GG-Gly(1:3)HNT50	2	6	0.025	1

The obtained hydrogels were poured into 24-well plates (15.6 mm well diameter) and crosslinked with $CaCl_2$ (0.025% w/v) using the external gelation method described by Kaklamani et al. (2014). Briefly, two parallel porous microcellulose sheets, previously soaked in $CaCl_2$, were placed at the top and bottom of the polymer, providing the Ca^{2+} ions required to promote a reproducible and uniform gelation of the polymer. After 24 h, the gelled samples destined to chemical, thermal and morphological analyses were obtained by freezing at -20 °C for 24 h, followed by freeze-drying for 48 h (Christ ALPHA 1-2/LD Plus, Martin Christ, Germany). Gelled samples employed for water uptake, mechanical and biological measurements were conditioned for 1 h in Phosphate-buffered

saline (PBS) solution prepared accordingly with Cold Spring Harbor Protocol. Samples used for the water uptake evaluation were dried as above mentioned.

2.3 Physico-chemical characterization

2.3.1 Scanning Electron Microscopy (SEM)

Scanning electron microscope (Hitachi TM3030 Tabletop SEM) equipped with Energy Dispersive Spectroscopy (EDS) was utilized to study the nanoclay dispersion into the composites, as well as its dried morphology. The samples were cut into small cylinders (1.5 cm of diameter and 2 cm of height), fixed on the aluminium stub using carbon tape. For pore size evaluation, 20 random pores from at least three SEM images were analyzed by ImageJ software.

2.3.2 Fourier Transform Infrared Spectroscopy in Attenuated Total Reflection mode (FT-IR/ATR)

FT-IR/ATR analysis was performed on a Spectrum Two PE instrument using the Universal ATR accessory (Single Reflection Diamond) (PerkinElmer Inc., Waltham, MA) at 4 cm-1 resolution. Dried samples were analyzed without any preliminary preparative step.

2.3.3 X-ray Photoelectron Spectroscopy (XPS)

XPS analysis was performed by a scanning microprobe PHI 5000 VersaProbe II (Physical Electronics, Chanhassen, MN), equipped with a monochromatized AlKα X-ray radiation source. The base pressure of the instrument to ensure vacuum in the analysis chamber was 10^{-9} mbar. The X-ray take-off angle was 45° and the samples were analyzed in HP mode (scanned size about 1400x200 μm). Survey scans (binding energy (BE) range 0–1200 eV, FAT mode, pass energy 117.4 eV) and high-resolution spectra (FAT mode, pass energy 29.35 eV) were recorded for each sample. Data analysis of the latter was performed using the MultiPak software package (version 9.6.1.7, which consists of a non-linear least-squares fitting program. The experimental points of the detailed spectra were fitted using Gaussian–Lorentzian peaks having the same full width at half maximum (FWHM). Charge referencing was performed by setting the lower binding energy C1s photo-peak (i.e., C1s hydrocarbon peak) at 284.8 eV. Quantification (atomic percentage, At%) was made using normalized peak area. The normalization of the peak area and comparison of data from different

elements was enabled by correction with empirically derived sensitivity factors according to MultiPak library.

2.3.4 Water uptake evaluation

Dried polymeric samples were firstly weighed (m_{di}), successively placed in tea bags. The tea bags containing the samples were sealed and immersed in PBS to determine the water uptake profile up to 24 hours at 37°C. The tea bags containing samples were weighted prior (m_i^0) and after each time point (m_i^t). Moreover, in order to guarantee that the amount of the measured water was only ascribable to the samples swelling, the weight of empty wet tea bags after each time point (m_b^t) was also considered. Therefore, the percentage of water uptake for each sample, along the time, was calculated using the Equation 1 reported below:

$$(WC\%)_i^t = \{[(m_i^t - m_b^t) - m_i^0]/m_{di}\}x100 \quad (1)$$

The test was performed in triplicate and results were reported as mean ± standard deviation.

2.3.5 Thermogravimetric Analysis (TGA)

Thermogravimetric measurements were carried out by TGA TA-Instrument Q500, (Waters S.p.A. Milan, Italy) in air atmosphere, following the thermic program: stabilisation at 30°C and isothermal scan at 10°C min^{-1} in the range 30-1000°C. Thermogravimetric (TG) and derivative thermogravimetric (DTG) curves were evaluated.

2.3.6 Mechanical tests: compression and stress-relaxation tests

Mechanical tests of the gellan-based hydrogels were performed using a mechanical testing machine (EZ-SX, Shimadzu, Japan). Test specimens were cylinder-shaped hydrogels with 1.6 cm diameter with an average height of around 2 cm. Compression resistance of five samples for each composition was evaluated at room temperature. The crosshead speed was set at 1 mm min^{-1}, and the load was applied until the specimen was compressed to around 35% of its original height before break. The compressive stress–strain curves were thus obtained from the average compressive modulus and standard deviation were calculated for each composition. Precisely, compressive

189 modulus was calculated as the slope of the initial linear portion of the stress–strain curve (0-15%),
190 as reported by Mattioli-Belmonte et al. (2015). Moreover, as previously described (Gentile et al.,
191 2012; Ciardelli et al., 2010; Pfeiffer et al., 2008) the values of collapse strength and strain (σ* and
192 e*, respectively) were calculated. For evaluating stress relaxation properties the hydrogels disks
193 were deformed with impermeable plates to a compressive strain of 10% with a deformation rate of
194 50 mm min^{-1}, in order to approximate an instantaneous deformation. Within 10% compression, the
195 stresses versus strain relations of the gels were almost linear. Subsequently, the strain was held
196 constant for 1200 s, while the load was recorded as a function of time. The obtained data were
197 analyzed using the software MATLAB R2015a. By fitting a third order exponential decay
198 (Equation 2) to the relaxation curves the three relaxation times were acquired. The increase in stress
199 during straining was not included when fitting the relaxation curves.

200 $$\sigma(t) = A1 * e^{-t/\tau_1} + A2 * e^{-t/\tau_2} + A3 * e^{-t/\tau_3} + y0 \quad (2)$$

201 Finally, in order to evaluate the viscosity of the gels, a first order exponential decay (Equation 3)
202 was fitted through the relaxation curves of every measurement.

203 $$\sigma(t) = A * e^{-t/\tau} + y0 \quad (3)$$

204 In particular, the viscosity (η) is found by multiplying the relaxation time τ with the linear modulus
205 E_0, obtained by fitting the initial linear part of the strain curve of the straining protocol and creating
206 a linear fit. The gels were tested as prepared and soaked in PBS during the stress-relaxation tests to
207 prevent dehydration (Zhao et al., 2010).

208 **2.4 Biological evaluation**

209 *2.4.1 Cell culture*

210 Neonatal Normal Human Dermal Fibroblasts (NHDF-Neo) were purchased from Lonza Biosciences
211 (Switzerland) and cultured as recommended by the seller. Briefly, fibroblasts were grown at 37°C,
212 5% CO_2, in Dulbecco's Modified Eagle Medium (DMEM, Sigma) supplemented with 10% fetal

bovine serum (FBS), 2 mM L-glutamine and a 1% antibiotic mixture containing penicillin and streptomycin (100 U mL^{-1}).

In order to perform biocompatibility assays, thin disks of gels (15 mm diameter and 25 of height) were prepared in 24-well plates and UV-sterilized for 15 min on each side. A further incubation with FBS was performed as previously described (Barbucci, 2009). A suspension of $2x10^4$ cells in DMEM was seeded dropwise on the top surface of gels and incubated at 37 °C, 5% CO_2 for 30 min. Then, fresh DMEM was added up to 500 µL volume.

2.4.2 Cell encapsulation

To encapsulate cells, the GG solutions were kept under agitation and slowly cooled until a temperature of 37 °C was reached. In a 24-multiwell plate, each sample solution was rapidly mixed with an equal volume of a cell suspension in warm DMEM. The final cell density was $2x10^5$ cells mL^{-1}. When the gelation occurred, the encapsulated hydrogels were covered with additional DMEM and incubated for 1, 3 and 7 days at 37°C.

2.4.3 Cytocompatibility studies

Cell viability was assessed with the live/dead staining (LIVE/DEAD® Cell Imaging Kit, Life Technologies, Thermo Scientific, USA) at days 1, 3 and 7. According to the manufacturer's protocol, samples were washed with phosphate buffered saline (PBS, Sigma-Aldrich, UK) and stained with 150 µL solution of 4 µM Ethidium homodimer-1 and 2 µM calcein in PBS. After 35 minutes of incubation at room temperature, cells were imaged with a Leica DM/LB fluorescence microscope using FITC and Rhodamine filters to detect calcein (ex/em 488 nm/515 nm) and Ethidium homodimer-1 (ex/em 570 nm/602 nm), respectively. The Presto Blue assay was exploited to test the metabolic activity of cells seeded on the gels after 1, 3, 5 and 7 days of culture. A LS-50B Luminescence Spectrometer (Perkin Elmer, Waltham, MA) was used to measure the fluorescence (560nm excitation and 590nm emission) after 5 h of incubation with a 10% aliquot of Presto Blue (Thermo Scientific, USA). The obtained values were corrected subtracting the average fluorescence of control wells. Histograms reported the percentage difference between samples and control

cultures. Results were expressed as mean ± standard deviation. Samples for fluorescence microscopy were fixed with paraformaldehyde 4% in PBS (15 min at room temperature), permeabilized washing them in PBS/0.1% Tween 20 and blocked in goat's serum 3% in PBS (1 h at room temperature). The samples were labelled with Phalloidin-FITC (Sigma, UK) for 20 min at RT to stain F-actin fibers. After PBS washings, nuclei were counterstained with 4',6-diamidino-2-phenylindole (VECTASHIELD® Antifade Mounting Medium with DAPI, VECTOR LABORATORIES LTS, UK). Samples were observed with an A1 Confocal Laser Microscope (Nikon, UK).

2.4.4 Statistical analysis

The significance of the results of PrestoBlue assay were assessed by a two-way repeated measures ANOVA. The test was replicated three times for each sample. All data were expressed as mean ± SD. Statistical analysis was performed with GraphPad Prism 7.01 software. The statistical differences between the tissue culture plastic control and the hydrogels were calculated using Dunnett test. Statistical significance was declared at *$p<0.05$, **$p<0.01$, ***$p<0.001$ and ****$p<0.0001$, where the asterisks labelled the samples with a cell metabolic activity significantly higher than the control.

3. Results and discussion

The physico-chemical characterization was carried out to evaluate the HNT influence and interaction within the polymeric gels. However, some tests were performed on dried samples that, during the PBS-conditioning and/or freeze-drying steps, lost not only water but also an appreciable amount of glycerol. Therefore, the glycerol content detected in dried samples by FT-IR/ATR, XPS and TGA techniques does not correspond to that present in the as prepared samples. Their mechanical properties have been studied, as well as their citocompatibility. The biological behavior of the hydrogels was evaluated for testing: (1) cell viability, metabolic activity and adhesion after seeding fibroblasts on the gel top surface and (2) their ability to encapsulate cells for future

applications in 3D printing. Finally, for a better comprehension of the work, we decided to add some figures/spectra of GG-Gly(1:1)HNTx samples in the *Supporting Information*, when they did not show any significant differences respect with GG-Gly(1:3)HNTx samples.

3.1. Physico-chemical characterization

3.1.1. Scanning electron microscopy (SEM)

In Figure 1A and Figure S1, the SEM micrographs of the freeze-dried gel cross-sections relevant to GG-Gly(1:3), GG-Gly(1:3)HNT10, Gly(1:3)HNT25 and GG-Gly(1:3)HNT50 were reported.

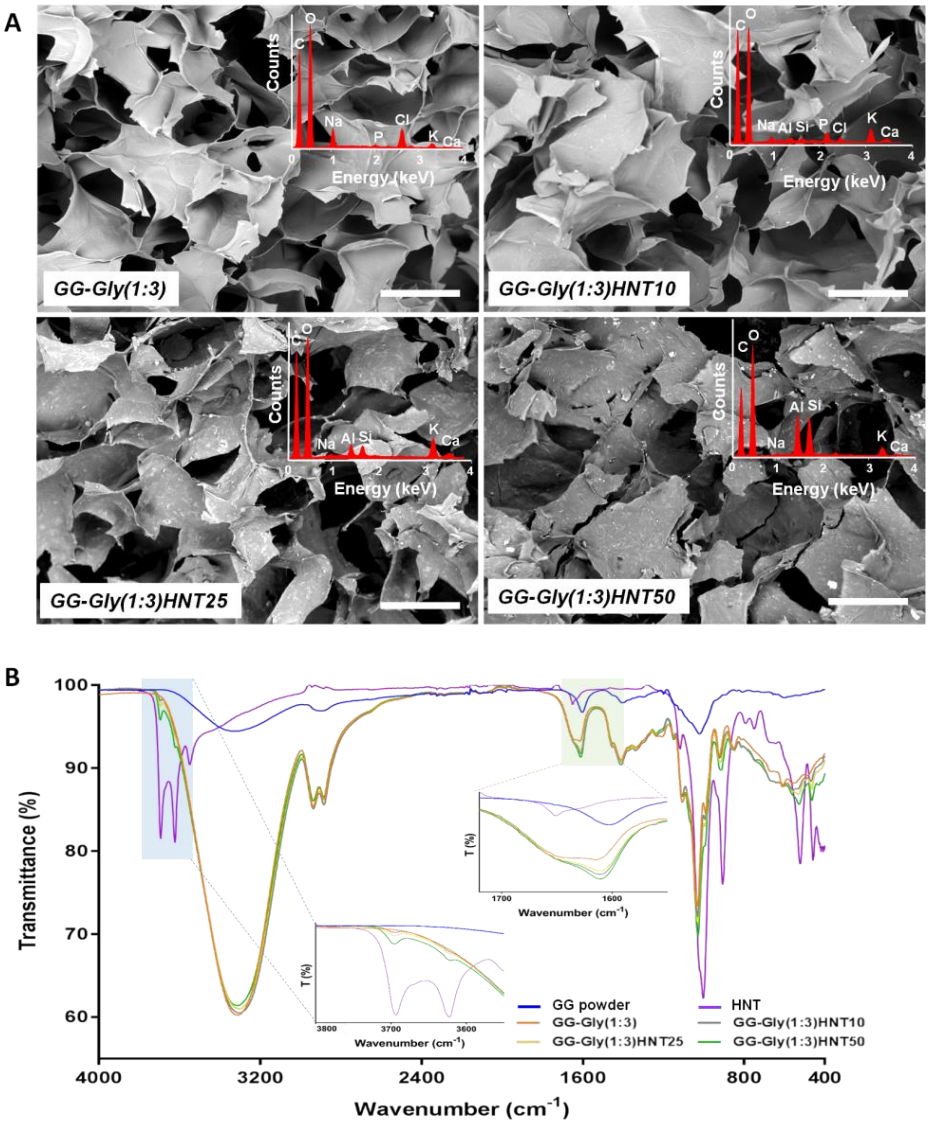

Figure 1. SEM/EDS and FT-IR/ATR characterization. (A) SEM micrographs of GG-Gly(1:3)HNTx samples, with x= 0, 10, 25 and 50. Scale bars: 500 μm. Insets: EDS spectra of the relevant samples. (B) FT-IR/ATR spectra of HNT and GG powders, and GG-Gly(1:3)HNTx samples, with x=0, 10, 25 and 50.

The SEM images provided insights into HNT dispersion within the polymeric network. No significant changes in the sample microarchitecture could be highlighted after HNT addition. The HNT presence was monitored through EDS analysis (see insets in Figure 1A and in Figure S1) by the calculation of the amount of aluminium and silicon, the characteristic elements of the nanotubes. Particularly, in the GG-Gly(1:3)HNT10 sample the relative aluminium abundance was 0.19 ± 0.04, while the silicon amount was 0.17± 0.04. For the GG-Gly(1:3)HNT25 sample, aluminium and silicon were 0.56 ± 0.07 and 0.51 ± 0.07. On the other hand, in the GG-Gly(1:3)HNT50 sample, the aluminium and silicon elements were respectively 2.6 ± 0.2 and 2.5 ± 0.2. However, at this concentration, the nanoclays were more prone to aggregate and their dispersion in the polymeric matrix was not as homogeneous as in GG-Gly(1:3)HNT10 and GG-Gly(1:3)HNT25 samples. Moreover, since the combination of the selected polymer, molecular spacer and nanoclay was not previously described, it was interesting to observe the texture achieved. The presence of glycerol may have a role in enhancing the porosity of the system, as it could be observed comparing the structure of all the other samples. Zhao et al. previously reported the impact of glycerol presence during fabrication of different polymeric scaffolds, describing its role as porogen molecule at the macroscopic level and as nanostructure ameliorant at the nanometric level. These effects were ascribed to a decrease in flexibility of glycerol-interacted polymer chains, that led to the reduction of polymeric conglomeration (Zhao et al., 2014). Finally, an evaluation of the sytems porosity was performed applying the same freeze-drying protocol for all the samples (see *par. 2.2.1*). GG-Gly(1:3) showed pores of around 365 ± 87 μm, while HNT addition had no impact onto the porosity, since the pore size for GG-Gly(1:3)HNT10, GG-Gly(1:3)HNT25 and GG-Gly(1:3)HNT50 were 290 ± 99, 314 ± 84 and 285 ± 82 μm respectively.

3.1.2. Fourier Transform Infrared Spectroscopy in Attenuated Total Reflection mode (FT-IR/ATR)

FT-IR/ATR spectra recorded on pure HNT and GG powder, and GG-Gly(1:3)HNTx (with x = 0, 10, 25 and 50) samples were shown in Figure 1B. GG powder and the GG-based samples spectra

showed the band at 3311 cm^{-1} due to the presence of –OH groups of glucopyranose ring. The band at 2899 cm^{-1} was due to the stretching vibrations of $–CH_2$ groups, while those appearing at 1602 and 1403 cm^{-1} were due to asymmetric and symmetric stretching of $–COO^-$ groups. The absorption band at 1145 cm^{-1} corresponded to antisymmetric C-O-C stretching of glycoside bonds, and the peak at around 1010 cm^{-1} was attributable to C-OH stretching. In the case of the GG-based samples crosslinked by Ca^{2+}, the presence of an additional band at 1656 cm^{-1}, visible as a shoulder on the left of the main C=O stretching band falling at 1611 cm^{-1} and absent in pure GG powder, suggested the interaction of $–COO^-$ groups with Ca^{2+} ions.

As far as HNT spectrum is concerned, the absorption peaks at 3693, 3622 and 1652 cm^{-1} can be associated to O-H stretching of inner hydroxyl groups and deformation of physiadsorbed water molecules, as already reported (Chen, 2016). These features were also evident in the GG-Gly(1:3)HNTx samples, in particular at higher HNT percentages (see insets in Figure 1B). Furthermore, the samples based on GG-Gly(1:1) presented similar information observed on the GG-Gly(1:3) series with only slight differences in the intensity of the chemical bands in the range 1500-1200 cm^{-1} and 1110-1000 cm^{-1}, due to the different glycerol content. Whereas, a more intense band (at about 1610 cm^{-1}) in the GG-Gly(1:1) than in GG-Gly(1:3) series was related to the relative higher GG weight in the composition of the former hydrogel (See Figure S2).

3.1.3. X-ray Photoelectron Spectroscopy (XPS)

XPS was employed to investigate the chemical composition of GG and HNT-containing hydrogels after freeze-drying. Atomic percentages (At%) recorded on the different samples were reported in Figure 2A. The analysis of GG powder showed the presence of the main elements of the polymer (i.e., carbon and oxygen), in addition to minor contributions (i.e., potassium, calcium, magnesium and sulfur), typical of gellan gum matrix as already reported by de Souza et al.(2016). For simplicity these minor elements, falling in the range of 0.4 – 2.0 At%, were not reported, while calcium signal, derived both from GG powder and the cross-linker, was considered. Beyond the abundance of carbon and oxygen, it is worth to note the presence of silicon and aluminium in the

HNT-containing samples whose signal area ratios were about 1, as expected on the basis of the HNT stoichiometry.

No XPS literature data are available on HNT-containing GG-based systems, therefore, an accurate curve fitting of C1s signals relevant to the investigated samples was carried out. In Figure 2B, high resolution C1s spectrum of GG-Gly(1:3)HNT25 was reported. No significant differences in C1s spectra relevant to the different HNT-based systems were detected. C1s spectra may be deconvoluted into five peak components associated with the following species: C-H (284.8 eV), C-COOR(H) (285.5 eV), C-OH (286.3 eV), O-C-O (287.7 eV) and COOR(H) (288.5 eV).

A

Sample	Atomic Percentage [%]				
	C1s	O1s	Ca2p	Si2p	Al2p
HNT	19.8	58.5	--	11.8	10.0
GG powder	59,7	39,1	1.2	--	--
GG	51.0	47.7	1.3	--	--
GG-Gly(1:1)	59.5	40.3	0.3	--	--
GG-Gly(1:1)HNT10	58.4	40.9	0.2	0.3	0.3
GG-Gly(1:1)HNT25	49.4	48.1	1.7	0.4	0.4
GG-Gly(1:1)HNT50	52.7	44.3	0.9	1.0	1.0
GG-Gly(1:3)	58.8	40.5	0.6	--	--
GG-Gly(1:3)HNT10	52.4	46.1	1.2	0.2	0.1
GG-Gly(1:3)HNT25	49.4	48.1	1.8	0.4	0.3
GG-Gly(1:3)HNT50	39.2	55.4	3.6	1.0	0.9

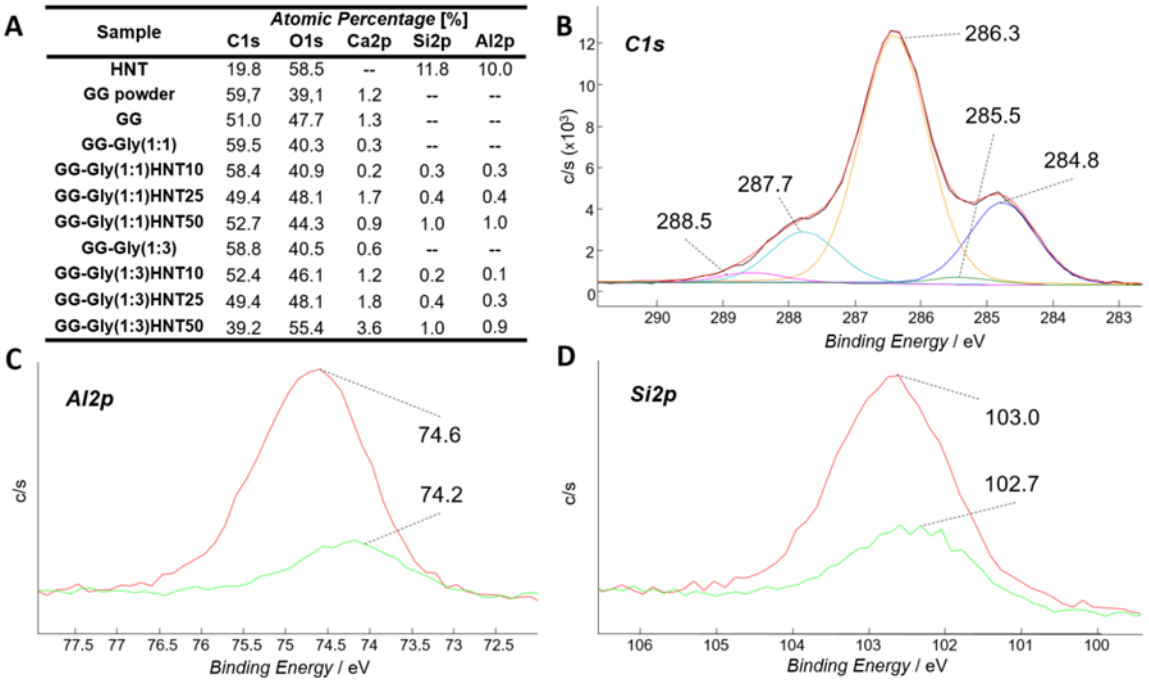

Figure 2. XPS Analysis. (A) Atomic percentages (At%) recorded on pure HNT (casted from an aqueous solution on Au sheet), GG powder and on freeze-dried GG, GG-Gly(1:1)HNTx and GG-Gly(1:3)HNTx (with x=0, 10, 25, and 50) samples. (B) XPS curve fitting of high resolution C1s spectrum related to GG-Gly(1:3)HNT25 sample. (C) High-resolution XPS spectra of aluminium in pure HNT (red) and GG-Gly(1:3)HNT50 sample (green). (D) High-resolution XPS spectra of silicon in pure HNT (red) and GG-Gly(1:3)HNT50 sample (green).

The first peak, attributed to aliphatic carbon, did not belong only to gellan matrix but also to sample contamination as a result of adsorbed hydrocarbons monolayers. The last peak was slightly shifted from 288.8 (typical of carboxylic acid groups) to 288.5 eV, indicating a coordination between Ca^{2+} and carboxylic acid groups, as already reported (Kang et al., 2015). Glycerol did not introduce

348 further peaks to C1s spectrum but its C-OH functionalities fell at 286.3 eV; anyway, its contribution
349 was markedly lower than that calculable from the starting amount due to the freeze-drying
350 procedure, as expected.
351 Figure 2C-D shows the high-resolution XPS spectra of aluminium and silicon in HNT (red line) and
352 GG-Gly(1:3)HNT50 sample (green line), where these contributions were more intense. It can be
353 observed a decrease (about 0.3-0.4 eV) in binding energy values of both silicon and aluminium
354 when HNT were loaded in the hydrogel matrix. This finding is related to the formation of hydrogen
355 bonds between the oxygen of Si-OH or Al-OH groups present in the nanoclays and hydrogen of the
356 organic network. A typical crystalline unit of HNT contains two types of hydroxyl groups, i.e., the
357 outer hydroxyl groups of the siloxane structure, where only a few of Si-OH groups are located in
358 HNT ends and surface defects, and the inner hydroxyl groups, due to the Al-OH groups situated in
359 the inner side. It can be hypothesized that the formation of hydrogen bonds between HNT and GG
360 and/or Gly involved not only most of the outer groups, but also the inner aluminols. An XPS
361 investigation of H-bond interactions in HNT-based polymer nanocomposites has been already
362 reported (Du et al., 2008), evidencing only interfacial interactions between the polymer matrix and
363 the Si-OH groups in HNT. In our case, glycerol intercalation into the HNT lumen could be invoked,
364 thus justifying the interaction between the inner Al-OH groups and glycerol hydroxyl groups (Liu et
365 al., 2011).
366 *3.1.4. Water uptake evaluation*
367 GG-based freeze-dried hydrogels were examined in terms of their swelling performances in PBS at
368 37 °C. Although the swelling measured on freeze-dried systems was not indicative of the real water
369 content of the as-prepared samples, this study allowed us to understand how the amount of HNT
370 can influence the water uptake properties of the proposed composites. The water uptake profile over
371 time of GG-Gly(1:3)HNTx specimens was reported in Figure 3A. The water uptake data at 24 hours
372 of all the examined samples were reported in Figure 3C. As shown in Figure 3A, the GG-Gly(1:3)-
373 based samples rapidly swelled upon contact with PBS, reaching a maximum just after five minutes

(i.e., around 800% and 1200% for samples with or without HNT respectively). This trend was observed also in the GG-Gly(1:1)HNTx series (Figure S3A). The presence of HNT, independently from their amount, was responsible in the GG-Gly(1:3) systems of an appreciable decrease of water uptake (reduction between 29 and 36%). Conversely, in the case of GG-Gly(1:1) samples, this reduction was lower (between 6 and 16%). These decreases in water uptake by the addition of HNT can be associated to the reduced hydrophilic polymer content in the composites (Huang et al., 2016). Indeed, the obtained water uptake in the 1:3 and 1:1 series meets the gellan gum content reported for freeze-dried samples.

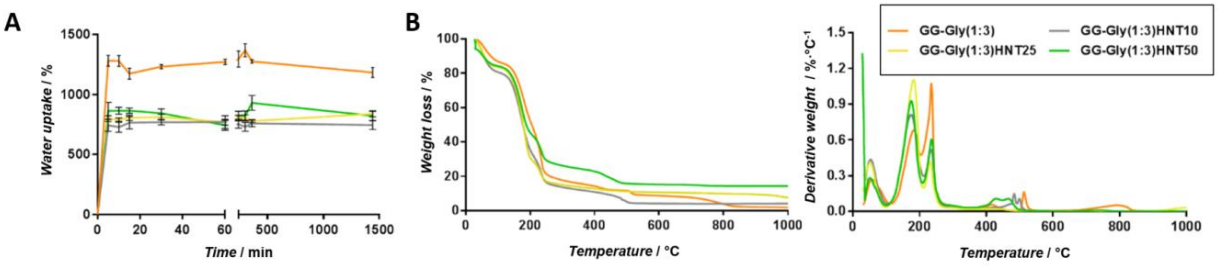

C

Sample	Swelling	Initial weight loss (moisture)		Glycerol Degradation		First degradation		Second degradation		Crystallized water in HNT		Third degradation		Fourth degradation		Residue
	Water uptake at 24h [%]	T [°C]	Weight %	T [°C]	Weight %	T [°C]	Weight %	T [°C]	Weight %	T [°C]	Weight %	T [°C]	Weight %	T [°C]	Weight %	Weight %
HNT	--	47.1	2.6	--	--	--	--	--	--	478.2	13.7	--	--	--	--	82.7
GG powder	--	54.6	11.0	--	--	240.1	52.4	411.8	15.3	--	--	559.2	10.8	919.6	3.0	7.5
GG	3160 ± 170	49.5	11.4	--	--	237.0	41.1	419.3	10.3	--	--	509.1	12.3	831.7	19.9	5.1
Gly	--	53.0	6.0	189.8	93.8	--	--	--	--	--	--	--	--	--	--	0.2
GG-Gly(1:1)	1570 ± 80	60.4	15.3	175.5	23.5	245.2	41.8	427.1	3.1	--	--	503.0	6.9	774.0	6.2	3.2
GG-Gly(1:1)HNT10	1320 ± 70	60.2	14.8	163.2	29.3	232.1	35.3	420.5	4.3	--	--	573.6	9.0	--	--	7.1
GG-Gly(1:1)HNT25	1470 ± 140	57.6	14.7	170.3	32.0	235.9	32.3	420.7	4.6	464.0	2.6	470.6	3.9	788.2	2.2	7.7
GG-Gly(1:1)HNT50	1320 ± 90	57.8	10.4	159.6	23.5	234.3	33.2	427.1	9.7	458.7	5.0	--	--	661.4	0.5	18.0
GG-Gly(1:3)	1180 ± 40	57.2	13.9	179.7	35.6	235.4	34.5	416.0	4.2	--	--	512.9	3.1	792.1	6.7	1.9
GG-Gly(1:3)HNT10	750 ± 40	55.2	18.5	173.3	48.9	234.2	19.2	421.9	3.1	483.5	3.5	499.2	1.8	--	--	4.1
GG-Gly(1:3)HNT25	840 ± 30	52.9	15.8	181.6	55.5	231.5	14.8	406.0	6.1	--	--	--	--	--	--	7.5
GG-Gly(1:3)HNT50	820 ± 40	52.2	15.5	174.3	40.7	236.3	19.3	427.1	5.4	468.2	3.5	--	--	761.6	1.2	14.3

Figure 3. Water uptake and Thermogravimetric Analysis. (A) Water uptake of GG-Gly(1:3)HNTx samples. (B) TGA and DTGA curves of GG-Gly(1:3)HNTx samples. (C) Water uptake data and thermal degradation steps of all the investigated samples.

It is interesting to note that, after swelling, GG-Gly samples released high amounts of water upon contacting with blotting paper while GG-Gly-HNT samples showed a significantly high water retention, as shown in the photograph reported in Figure S3B. Since in both bare and HNT-loaded gels a comparable pore size was observed (see Figure 1A), the higher water retention capability of

HNT-loaded gels could be ascribed to a water intercalation into the HNT lumen. This feature makes the proposed hydrogel an intriguing candidate as drug delivery system (Gupta & Shivakumar, 2010): the mesoporous HNT architecture could be exploited to intercalate different bioactive molecules, delaying the release kinetics typical of highly porous polymers.

3.1.5. Thermogravimetric Analysis (TGA)

The overlay of TG (on the left) and DTG (on the right) signals, recorded on GG-Gly(1:3)HNTx (with x=0,10,25 and 50) were reported in Figure 3B. The degradation steps, with the relevant temperatures and weight loss percentages, were reported in Figure 3C for all examined samples (i.e., the starting materials and the GG-Gly(1:1)HNTx and GG-Gly(1:3)HNTx series).

In particular, the GG powder thermogram indicated a weight loss of 11%, in the temperature range from room to about 200°C, due to the water removal. The main degradation temperature was centred at about 240°C. This first step of degradation promoted a weight loss of 52%, while the next two steps promoted a weight loss of 15% at 412°C, relevant to loss of volatile components and rupture of chain, and a weight loss of 11% at 559°C, relevant to fragmentation into monomers (monosaccharide units). A fourth degradation step occurred at about 920°C (weight loss = 3%). The remaining residue was of 7.5% of the initial weight of the sample. With regard to the GG based sample, obtained by crosslinking with Ca^{2+} ions, the thermogram showed a weight loss of 11% due to the water removal. The main degradation temperature was 237°C, with a weight loss of 41%. The weight loss of crosslinked GG in the first stage decreased, indicating that the thermostability was improved after the addition of the crosslinking agent. The next two steps promoted a weight loss of 10% at 419°C and 12% at 509°C, respectively. Finally, the last degradation step occurred at about 832°C, with a weight loss equal to 20%. The remaining residue was equal to 5% of the initial weight of the sample.

The addition of glycerol in the samples, at different GG:Gly ratios (i.e., 1:1 and 1:3), was responsible of the presence of an additional peak in the range 160-180°C, relevant to the vaporization of Gly (that in pure glycerol occurred at 190°C). This thermal event caused a weight

loss of 24 and 36% in GG-Gly(1:1) and GG-Gly(1:3), respectively. Furthermore, as also reported in XPS characterization, due to the freeze-drying procedure, the Gly contribution was markedly lower than that calculable from the starting amounts.

The HNT thermogram (plot not shown) exhibited a weight loss of 3.5% in the temperature range from room to about 170°C, which was due to the loss of water and/or volatile compounds. The main HNT mass loss of about 14%, centred at the temperature range of 478°C, was attributed to the release of crystallization water (Jia et al., 2009). The residue at 1000°C in air was equal to 83%. The HNT-containing samples revealed a residue at 1000°C in good agreement with their HNT feed ratio (see the TG on the left of Figure 3B). Furthermore, in HNT-containing samples the glycerol amount was markedly higher than in those without HNT. This finding substantiated the hypothesis of hydrogen bonds formation between HNT hydroxyl groups and glycerol, observed by XPS analysis.

3.1.6. Mechanical tests

The mechanical properties of the obtained hydrogels were tested using a mechanical testing machine. Figure 4A showed the stress-strain curve obtained by the compression test at strain of 0-25%. During the test, the hydrogels did not break but they underwent densifications. As described previously by Gentile et al. (2012) the values of elastic modulus (*E*), collapse strength and strain (σ^* and ε^* respectively) were calculated from the curves and listed in Figure 4C. A significant improvement of the compressive modulus was observed by adding HNT (up to 25%) into the polymeric gel (70.5 ± 6.8 kPa for GG-Gly(1:3)HNT25 compared with 48.5 ± 5.3 kPa for GG-Gly(1:3)). The obtained values are higher or within the range of mechanical properties described for other hydrogels proposed for soft tissue regeneration (Nettles et al., 2004; Balakrishnan et al., 2014).

This mechanical reinforcement effect can be attributed to an additional energy-dissipating mechanism introduced by the nanotubes in the polymeric gels. Recent molecular dynamics studies suggested that this additional dissipative mechanism is a result of the mobility of the nanofillers.

During the deformation process, the HNT may orient and align under compression stress, creating temporary cross-links between polymer chains, thereby creating a local region of enhanced strength (Shah et al., 2005). However, when the amount of the nanotubes content increased, as in the GG-Gly(1:3)HNT50, they became less mobile. Therefore, the ability of the HNT to dissipate energy is also reduced, resulting in almost no improvement in the toughness of the material (34.3 ± 2.6 kPa). Furthermore the systems with higher Gly content demonstrated to be stiffer than those prepared with GG-Gly(1:1) with a maximum increase of 2.5-fold for the system containing 25% HNT (70.5 ± 6.8 kPa for GG-Gly(1:3) respect with 28.7 ± 2.6 kPa for for GG-Gly(1:1)).

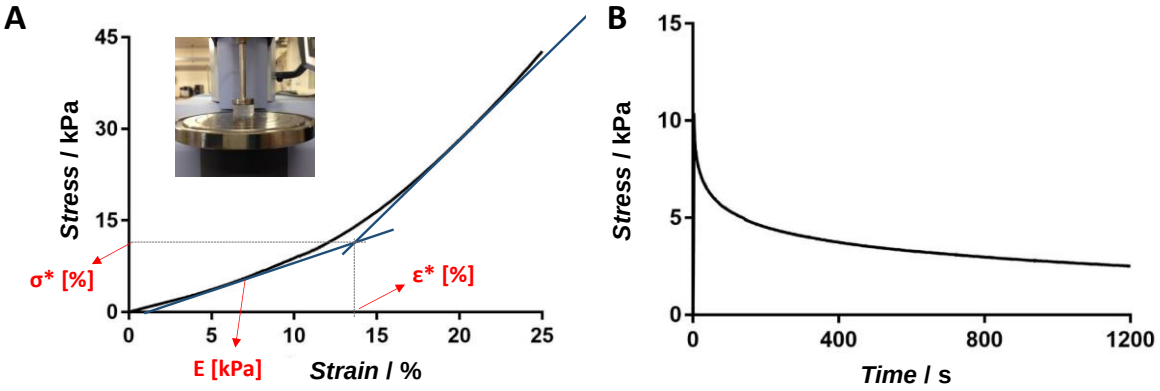

C

Sample Code	E [kPa]	σ* [kPa]	ε* [%]	τ_1 [s]	T_2 [s]	T_3 [s]	η [MPa.s]
GG-Gly(1:1)	28.1 ± 3.7	8.7 ± 1.2	15.1 ± 2.0	6.7 ± 1.0	67 ± 17	479 ± 29	24.6 ± 3.2
GG-Gly(1:1)HNT10	26.6 ± 1.6	9.3 ± 1.3	14.8 ± 1.7	7.9 ± 1.4	72 ± 20	589 ± 59	25.9 ± 0.9
GG-Gly(1:1)HNT25	28.7 ± 2.6	10.4 ± 1.6	13.8 ± 2.2	8.0 ± 2.1	86 ± 21	605 ± 40	25.9 ± 0.3
GG-Gly(1:1)HNT50	20.7 ± 2.4	8.7 ± 1.6	13.9 ± 2.6	6.5 ± 1.1	61 ± 19	454 ± 39	26.2 ± 0.6
GG-Gly(1:3)	48.5 ± 5.3	9.5 ± 2.1	15.5 ± 2.3	7.9 ± 2.0	89 ± 20	789 ± 59	26.9 ± 2.0
GG-Gly(1:3)HNT10	48.7 ± 3.5	10.3 ± 1.5	14.9 ± 2.2	8.3 ± 2.2	93 ± 23	865 ± 63	27.2 ± 1.1
GG-Gly(1:3)HNT25	70.5 ± 6.8	12.5 ± 1.8	13.9 ± 1.8	8.6 ± 2.1	113 ± 22	1010 ± 79	30.1 ± 2.0
GG-Gly(1:3)HNT50	34.3 ± 2.6	10.5 ± 1.4	14.3 ± 2.0	8.1 ± 1.8	97 ± 18	655 ± 61	28.9 ± 1.9

Figure 4. Mechanical characterization. (A) Stress-strain curve obtained by compression test. (B) stress-relaxation curve. (C) Elastic modulus (E), collapse strength (σ*), collapse strain (ε*), relaxation times (τ_1, τ_2 and τ_3) and viscosity (η) calculated for the prepared hydrogels.

This effect has been described also by Lugao et al. (2002) where glycerol, added to polyvinyl pyrrolidone hydrogels for wound healing applications, increased the elasticity of the gels as a result of the plasticising effect. Given the nature of the time dependent response of hydrogels, in addition

to simple tests at fixed rate, the samples were subjected to relaxation (load decrease at fixed strain) experiments, where variation in response with time is of interest and the loading is fixed, in order to evaluate the viscoelasticity behavior. These properties are fundamental, in combination with the mechanical stiffness, to influence cell behavior as described recently by Chaudhuri et al. (2016) where they studied how to regulate mesenchymal stem cell fate in hydrogels with tunable stress relaxation. Figure 4B shows the typical stress relaxation curve obtained after 1200 s and the relaxation times and viscosity values are listed in Figure 4C. Each material showed a two-stage stress relaxation response: a fast decrease in stress for short times after the step strain, followed by a slow relaxation covering a couple of decades of time. A generalized Maxwell model was used to investigate whether the behavior could be explained by linear viscoelasticity, providing a range of relaxation times and associated amplitudes that can approximate the viscoelastic behavior of biological materials.

In literature, the generalized Maxwell model developed consisted of three relaxation times (τ_1 = 1-10 s, τ_2 = 10-100 s and τ_3 > 1000 s) for modelling soft biological tissues (Wagenseil et al., 2003). In our work, relaxation times ranging from τ_1 = 6-9 s, τ_2 = 60-120 s and τ_3 = 600-1100 s were comparable with the literature. Finally, it was observed that the addition of HNT did not influence significantly the viscosity of the composite hydrogels (26.9 ± 2.0 MPa.s for GG-Gly(1:3) and 30.1 ± 2.0 MPa.s for GG-Gly(1:3)HNT25). However, the gels with higher content of glycerol revealed to be more viscous comparing each system with the same content of HNT (25.9 ± 0.3 MPa.s for GG-Gly(1:1)HNT25), due to the intrinsic glycerol capability to increase the viscosity of aqueous solutions. Indeed, the addition of glycerol to synthetic and natural polymers enhanced hydrogels viscosity, as already reported in literature (Fernandez-Dıaz et al., 2001;Payen, 2007).

3.2. Biological tests

3.2.1. Biocompatibility of the HNT-loaded hydrogels

NHDF-Neo were seeded onto the surface of GG, GG-Gly (1:1)HNTx and GG-Gly (1:3)HNTx hydrogels in order to evaluate the cytocompatibility of these materials. Cell viability was evaluated after 1, 3 and 7 days by live/dead assay, as shown in Figure 5 and S3.

The bare gellan gum matrix GG showed a low cell viability and poor ability to promote cell attachment. As reported in literature (Shin et al., 2014), the lack of adhesive signals in gellan gum material do not favour cellular adhesion.. However, the addition of glycerol improved cell survival on all the GG-Gly hydrogels studied. Furthermore, , it was found that the HNT addition to GG-Gly hydrogels enhanced the cell viability, thanks to their biocompatibility and the increase in surface roughness (Figure 6B) (Zhou et al., 2010; Kommireddy et al., 2005; Hughes et al., 2015; Huang et al., 2016).

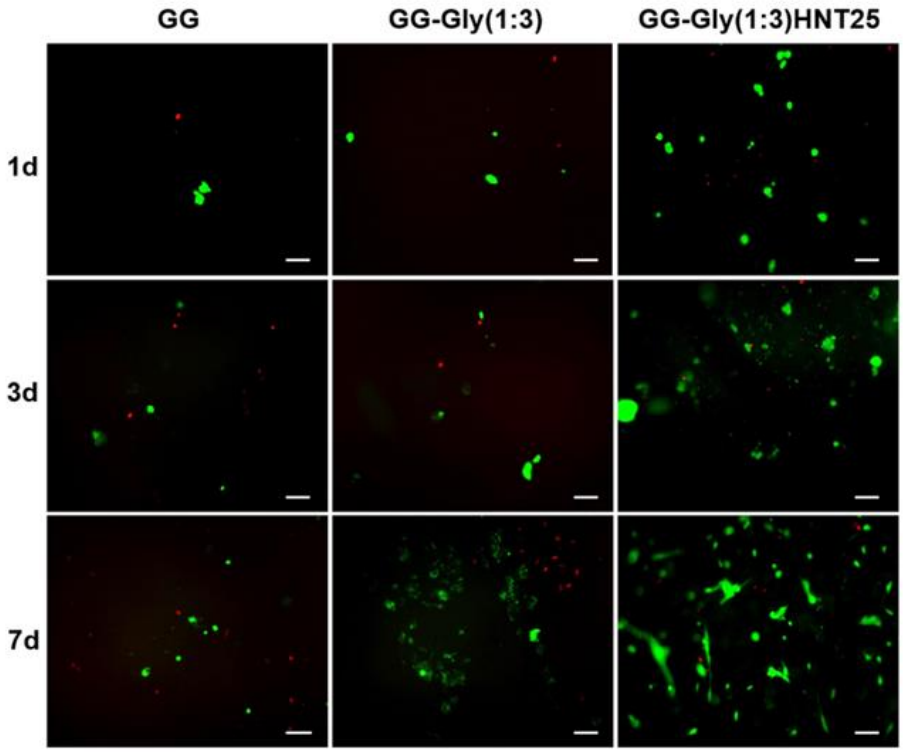

Figure 5. Live/Dead assay of cells seeded on hydrogel surfaces. Representative fluorescent micrographs of live (green) and dead (red) cells seeded on GG, GG-Gly(1:3) and GG-Gly(1:3)HNT25 after 1, 3 and 7 days of culture. Scale bars 200 μm.

As shown on the surface of GG-Gly(1:3)HNT25 sample, cell viability was maintained and cell growth was enhanced at each time point (up to 7 days), as observed by the Live/dead and metabolic activity assays. Therefore, cell behavior seemed to be led by the combination of mechanical properties and HNT content.

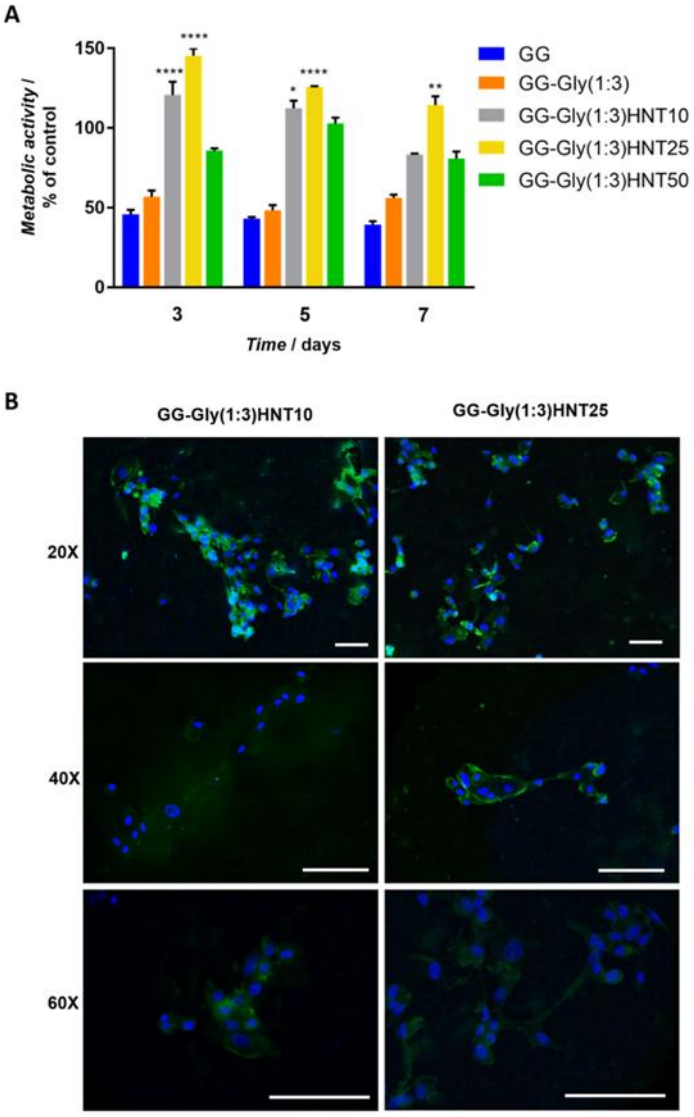

Figure 6. Metabolic activity and morphological study of cells seeded on hydrogel surfaces. (A) PrestoBlue assay of cells cultured on GG and GG-Gly(1:3)HNTx hydrogels for 3, 5 and 7 days. (B) Fluorescence microscopy images of cells seeded on GG-Gly(1:3)HNT10 and GG-Gly(1:3)HNT25 after 3 days of culture. Scale bars: 100 µm.

The metabolic activity of NHDF-Neo was evaluated using Presto Blue assay (Figure 6A and S4), normalized by control (cells seeded onto tissue culture plastic) at each incubation time-point. These

data confirmed the results observed by the live/dead assay, where glycerol presence led to an increase in cellular metabolic activity when compared to the bare GG hydrogel ($p<0.05$). Glycerol plays essential roles in several intracellular metabolic pathways (i.e., it forms the backbone of fats such as triglycerides, and/or takes part in glycolysis or glycogenesis processes) and has been exploited as a low-cost and biocompatible monomer to design scaffolds for tissue engineering (Barrett et al., 2009). NHDF-Neo metabolic activity revealed a significant increase at each time point by incorporating HNT within the GG:Gly hydrogel in different ratios, as seen for GG-Gly (1:3)HNTx and GG-Gly (1:1)HNTx in Figure 6A and S4.

Interestingly, the hydrogel GG-Gly(1:3)HNT25 induced the highest fibroblasts metabolic activity when compared to GG, GG-Gly, GG-Gly(1:3)HNT10 and GG-Gly(1:3)HNT50 ($p<0.001$). Similar results to those obtained for HNT-containing GG-Gly hydrogels were observed on halloysite-doped dental scaffolds (Lvov et al., 2016; Vergaro et al., 2010). The HNT-loaded samples stimulated the growth and promoted a faster fibroblasts spreading. However, a significant viability reduction was observed on hydrogels with high HNT content (GG-Gly(1:3)HNT50), this can be explained by a potential adverse effect of a concentrated halloysite, as described elsewhere (Lvov et al., 2016; Vergaro et al., 2010).

Due to the best cell viability and metabolic activity performance, the fibroblast phenotype was studied by fluorescence microscopy on GG-Gly(1:3)HNT25 and GG-Gly(1:3)HNT10 samples. After 3 days of culture, NHDF-Neo exhibited their typically flattened and elongated morphology on both hydrogels, spreading homogeneously along the sample surface and establishing many intercellular contacts (Figure 6B).

3.2.2. Cells encapsulated

The NHDF-Neo were encapsulated within the GG-Gly hydrogels containing HNT and compared with GG and GG:Gly control hydrogels. The cell viability of encapsulated cells within the different hydrogels was assessed at 1, 3 and 7 days by Live/Dead assay (Figure 7 and Figure S6). The cells

encapsulated within the diverse systems showed a similar viability response to those observed when seeded on the hydrogels surface (Figure 5).

A higher cell viability was detected within HNT-loaded samples in comparison with the bare GG and GG-Gly hydrogels along the incubation period. It has been demonstrated that hydrogels stiffness, microstructures and porosity, and material nature influence cellular functions such as cells attachment and proliferation (Goponenko & Dzenis, 2016). As shown previously, the incorporation of HNT enhanced the mechanical properties of the GG-Gly hydrogels and also improved the biocompatibility of this material. Since cells were confined within the hydrogel matrix, no matter how soft or stiff, the limited cell traction forces with substrate led to rounded cell morphology, either within GG-Gly hydrogel and/or in presence of HNT.

This phenomenon has been widely reported in advanced 3D culture studies (Peyton & Putnam, 2005; Huebsch et al., 2010; Khetan et al., 2013; Murphy et al., 2014).

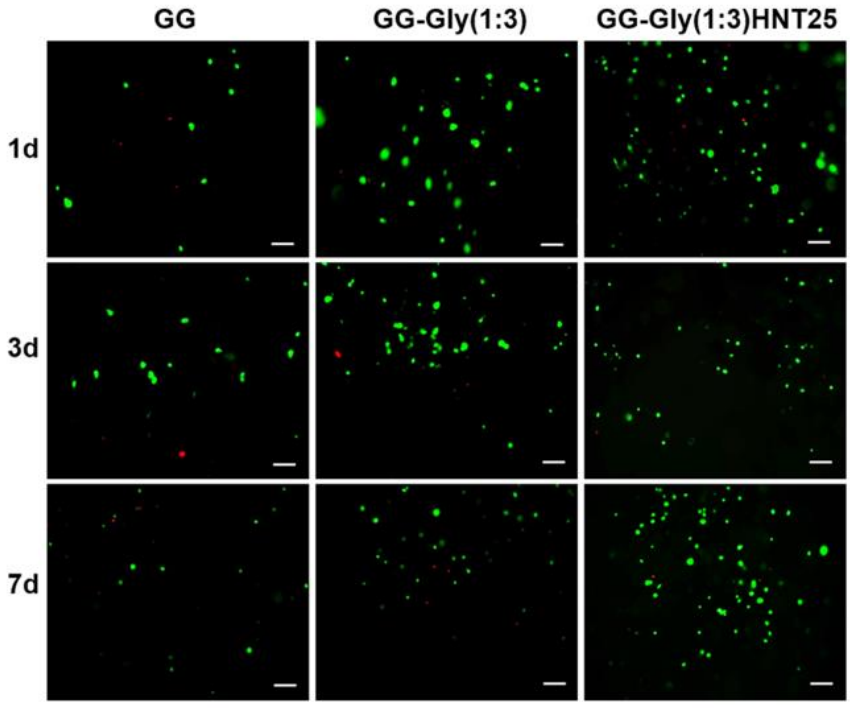

Figure 7. Live/Dead assay of hydrogel-encapsulated cells. Representative fluorescent micrographs of live (green) and dead (red) cells encapsulated in GG, GG-Gly(1:3) and GG-Gly(1:3)HNT25 after 1, 3 and 7 days of culture. Scale bars 200 μm.

4. Conclusions

Halloysite nanotubes have been integrated in gellan gum matrices to develop composite hydrogels with tunable physical features, showing a good Human Dermal Fibroblasts biocompatibility when cells were seeded on the top of the gels or encapsulated within the polymeric matrix. Fibroblasts onto hydrogels with 25% HNT displayed the highest metabolic activity, which could be related to the hydrogel mechanical and topographical features led by the HNT content. Gels presented suitable mechanical properties to develop hydrogels scaffolds or injectable materials for different soft tissue engineering applications (i.e. pancreas, liver, skin and chondral regeneration). Furthermore, the hydrogels could be exploited to design *in vitro* cell culture systems and tissue models to study cell behavior and interactions, mimicking the native microenvironments. In future, differentiation routes of mesenchymal stem cells will be investigated, considering also the opportunity to functionalize the HNT surface and mesoporous lumen with bioactive molecules able to elicit *in situ* advantageous cell responses.

Acknowledgments

This work was supported by Università degli Studi di Bari Aldo Moro. Dr P. Gentile and Dr Ana M. Ferreira are member of the UK EPSRC Centre for Innovative Manufacturing of Medical Devices (MeDe Innovation, EPSRC grant EP/K029592/1). The authors would like to thank the Bioimaging Unit at Newcastle University for supporting the confocal analysis. Dr Vincenzo Schiavo is greatly acknowledged for his valuable support in TGA measurements. The authors would also like to thank Mr Michael Foster for his helpful advice on SEM/EDX analysis, Mr Stephen Moore for the kind support during the freeze-drying procedure and Mr Alex Boote for his helpful contribution in mechanical test.

References

Annabi, N., Tamayol, A., Uquillas, J.A., Akbari, M., Bertassoni, L.E., Cha, C., Camci-Unal, G., Dokmeci, M.R., Peppas, N.A., Khademhosseini, A. (2014). 25th anniversary article: rational design and applications of hydrogels in regenerative medicine. *Advanced Materials, 26,* 85-124.

Balakrishnan, B., Joshi, N., Jayakrishnan, A., Banerjee, R. (2014). Self-crosslinked oxidized alginate/gelatin hydrogel as injectable, adhesive biomimetic scaffolds for cartilage regeneration. *Acta biomaterialia, 10,* 3650-63.

Barbucci, R. (2009). *Hydrogels: Biological properties and applications*, Milão: Springer, (Chapter 8, p. 84).

Barrett, D.G., Yousaf, M.N. (2009). Design and applications of biodegradable polyester tissue scaffolds based on endogenous monomers found in human metabolism. *Molecules, 14,* 4022-50.

Bottino, M.C., Yassen, G.H., Platt, J.A., Labban, N., Windsor, L.J., Spolnik, K.J., Bressiani, A.H.A. (2015). A novel three-dimensional scaffold for regenerative endodontics: materials and biological characterizations. *Journal of tissue engineering and regenerative medicine, 9,* E116-E23.

Cerqueira, M.T., da Silva, L.P., Santos, T.C., Pirraco, R.r.P., Correlo, V.M., Reis, R.L., Marques, A.P. (2014). Gellan gum-hyaluronic acid spongy-like hydrogels and cells from adipose tissue synergize promoting neoskin vascularization. *ACS applied materials & interfaces, 6,* 19668-79.

Chalasani, R., Gupta, A., Vasudevan, S. (2013). Engineering new layered solids from exfoliated inorganics: a periodically alternating hydrotalcite-montmorillonite layered hybrid. *Scientific reports, 3, 3498.*

Chaudhuri, O., Gu, L., Klumpers, D., Darnell, M., Bencherif, S.A., Weaver, J.C., Huebsch, N., Lee, H.P., Lippens, E., Duda, G.N. (2016). Hydrogels with tunable stress relaxation regulate stem cell fate and activity. *Nature materials, 15,* 326-34.

Chen, F.M., Liu, X. (2016). Advancing biomaterials of human origin for tissue engineering. *Progress in polymer science*, *53*, 86-168.

Ciardelli, G., Gentile, P., Chiono, V., Mattioli-Belmonte, M., Vozzi, G., Barbani, N., Giusti, P. (2010). Enzymatically crosslinked porous composite matrices for bone tissue regeneration. *Journal of Biomedical Materials Research Part A*, *92*, 137-51.

Coutinho, D.F., Sant, S.V., Shin, H., Oliveira, J.T., Gomes, M.E., Neves, N.M., Khademhosseini, A., Reis, R.L. (2010). Modified Gellan Gum hydrogels with tunable physical and mechanical properties. *Biomaterials*, *31*, 7494-502.

da Silva, L.P., Cerqueira, M.T., Sousa, R.A., Reis, R.L., Correlo, V.M., Marques, A.P. (2014). Engineering cell-adhesive gellan gum spongy-like hydrogels for regenerative medicine purposes. *Acta biomaterialia*, *10*, 4787-97.

Dawson, J.I., Oreffo, R.O.C. (2013). Clay: new opportunities for tissue regeneration and biomaterial design. *Advanced Materials*, *25*, 4069-86.

De Giglio, E., Cometa, S., Ricci, M.A., Cafagna, D., Savino, A.M., Sabbatini, L., Orciani, M., Ceci, E., Novello, L., Tantillo, G.M. (2011). Ciprofloxacin-modified electrosynthesized hydrogel coatings to prevent titanium-implant-associated infections. *Acta biomaterialia*, *7*, 882-91.

de Souza, F.S., de Mello Ferreira, I.L., da Silva Costa, M.A., de Lima, A.L.F., da Costa, M.P.M., da Silva, G. M. (2016). Evaluation of different methods to prepare superabsorbent hydrogels based on deacetylated gellan. *Carbohydrate polymers*, *148*, 309-17.

Du, M., Guo, B., Lei, Y., Liu, M., Jia, D. (2008). Carboxylated butadiene–styrene rubber/halloysite nanotube nanocomposites: interfacial interaction and performance. *Polymer*, *49*, 4871-6.

Du, M., Guo, B., Jia, D. (2010). Newly emerging applications of halloysite nanotubes: a review. *Polymer International*, *59*, 574-82.

Fernandez-Dıaz, M.D., Montero, P., Gomez-Guillen, M.C. (2001). Gel properties of collagens from skins of cod (Gadus morhua) and hake (Merluccius merluccius) and their

627 modification by the coenhancers magnesium sulphate, glycerol and transglutaminase. *Food*
628 *Chemistry, 74*, 161-7.
629 Gentile, P., Mattioli-Belmonte, M., Chiono, V., Ferretti, C., Baino, F., Tonda-Turo, C.,
630 Vitale-Brovarone, C., Pashkuleva, I., Reis, R.L., Ciardelli, G. (2012). Bioactive glass/polymer
631 composite scaffolds mimicking bone tissue. *Journal of Biomedical Materials Research Part A*, *100*,
632 2654-67.
633 Giavasis, I., Harvey, L.M., McNeil, B. (2000). Gellan gum. Critical reviews in
634 biotechnology. *Critical reviews in biotechnology*, *20*, 177-211.
635 Goponenko, A.V., Dzenis, Y.A. (2016) Role of mechanical factors in applications of
636 stimuli-responsive polymer gels–Status and prospects. *Polymer*, *101*, 415-449.
637 Gorodzha, S. Douglas, T.E.L., Samal, S.K., Detsch, R., Cholewa-Kowalska, K.,
638 Braeckmans, K., Boccaccini, A.R., Skirtach, A.G., Weinhardt, V., Baumbach, T. (2016). High-
639 resolution synchrotron X-ray analysis of bioglass-enriched hydrogels. *Journal of Biomedical*
640 *Materials Research Part A, 104*, 1294-201.
641 Gupta, N.V., Shivakumar, H.G. (2010). Preparation and characterization of superporous
642 hydrogels as gastroretentive drug delivery system for rosiglitazone maleate. *Daru*, *18*, 200-10.
643 Huang, B., Liu, M., Long, Z., Shen, Y., Zhou, C. (2016). Effects of halloysite nanotubes on
644 physical properties and cytocompatibility of alginate composite hydrogels. *Materials Science and*
645 *Engineering: C*, *70*, 303-310.
646 Huebsch, N., Arany, P.R., Mao, A.S., Shvartsman, D., Ali, O.A., Bencherif, S.A., Rivera-
647 Feliciano, J., Mooney, D.J. (2010). Harnessing traction-mediated manipulation of the cell/matrix
648 interface to control stem-cell fate. *Nature materials*, *9*, 518-26.
649 Hughes, A.D., Marsh, G., Waugh, R.E., Foster, D.G., King, M.R. (2015). Halloysite
650 nanotube coatings suppress leukocyte spreading. *Langmuir*, *31*, 13553-60.

Jia, Z., Luo, Y., Guo, B., Yang, B., Du, M., Jia, D. (2009). Reinforcing and flame-retardant effects of halloysite nanotubes on LLDPE. *Polymer-Plastics Technology and Engineering*, *48*, 607-13.

Kaklamani, G., Cheneler, D., Grover, L.M., Adams, M.J., Bowen, J. (2014). Mechanical properties of alginate hydrogels manufactured using external gelation. *Journal of the mechanical behavior of biomedical materials*, *36*, 135-42.

Kamble, R., Ghag, M., Gaikawad, S., Panda, B.K. (2012). Halloysite Nanotubes and Applications: A Review. *Journal of Advanced Scientific Research*, *3*, 25-29.

Kang, D., Cai, Z., Jin, Q., Zhang, H. (2015). Bio-inspired composite films with integrative properties based on the self-assembly of gellan gum–graphene oxide crosslinked nanohybrid building blocks. *Carbon*, *91*, 445-57.

Khetan, S., Guvendiren, M., Legant, W.R., Cohen, D.M., Chen, C.S., Burdick, J.A. (2013). Degradation-mediated cellular traction directs stem cell fate in covalently crosslinked three-dimensional hydrogels. *Nature materials*, *12*, 458-65.

Kommireddy, D.S., Ichinose, I., Lvov, Y.M., Mills, D.K. (2005). Nanoparticle multilayers: Surface modification for cell attachment and growth. *Journal of Biomedical Nanotechnology*, *1*, 286-90.

Liu, H., Chaudhary, D., Yusa, S.I., Tadé, M.O. (2011). Glycerol/starch/Na^+-montmorillonite nanocomposites: a XRD, FTIR, DSC and 1 H NMR study. *Carbohydrate Polymers*, *83*, 1591-7.

Liu, M., Zhang, Y., Wu, C., Xiong, S., Zhou, C. (2012). Chitosan/halloysite nanotubes bionanocomposites: structure, mechanical properties and biocompatibility. *International journal of biological macromolecules*, *51*, 566-75.

Liu, M., Wu, C., Jiao, Y., Xiong, S., Zhou, C. (2013). Chitosan–halloysite nanotubes nanocomposite scaffolds for tissue engineering. *Journal of Materials Chemistry B*, *1*, 2078-89.

675 Liu, M., Dai, L., Shi, H., Xiong, S., Zhou, C. (2015). In vitro evaluation of
676 alginate/halloysite nanotube composite scaffolds for tissue engineering. *Materials Science and*
677 *Engineering: C, 49*, 700-12.
678 Lopes, A.C., Martins, P., Lanceros-Mendez, S. (2014). Aluminosilicate and aluminosilicate
679 based polymer composites: present status, applications and future trends. *Progress in Surface*
680 *Science 89*, 239-77.
681 Lugão, A.B., Rogero, S.O., Malmonge, S.M. (2002). Rheological behaviour of irradiated
682 wound dressing poly (vinyl pyrrolidone) hydrogels. *Radiation Physics and Chemistry, 63*, 543-6.
683 Lvov, Y., Wang, W., Zhang, L., Fakhrullin, R. (2016). Halloysite clay nanotubes for loading
684 and sustained release of functional compounds. *Advanced Materials, 28*, 1227-50.
685 Mattioli-Belmonte, M., De Maria, C., Vitale-Brovarone, C., Baino, F., Dicarlo, M., Vozzi,
686 G. (2015). Pressure-activated microsyringe (PAM) fabrication of bioactive glass–poly (lactic-co-
687 glycolic acid) composite scaffolds for bone tissue regeneration. *Journal of tissue engineering and*
688 *regenerative medicine*.
689 Murphy, W.L., McDevitt, T.C., Engler, A.J. (2014). Materials as stem cell regulators.
690 *Nature materials, 13*, 547-57.
691 Naumenko, E.A., Guryanov, I.D., Yendluri, R., Lvov, Y.M., Fakhrullin, R.F. (2016). Clay
692 nanotube–biopolymer composite scaffolds for tissue engineering. *Nanoscale, 8*, 7257-71.
693 Nettles, D.L., Vail, T.P., Morgan, M.T., Grinstaff, M.W., Setton, L.A. (2004).
694 Photocrosslinkable hyaluronan as a scaffold for articular cartilage repair. *Annals of biomedical*
695 *engineering, 32*, 391-7.
696 Oliveira, M.B., Custódio, C.A., Gasperini, L., Reis, R.L., Mano, J.F. (2016). Autonomous
697 osteogenic differentiation of hASCs encapsulated in methacrylated gellan-gum hydrogels. *Acta*
698 *biomaterialia, 41*, 119-32.
699 Osmałek, T., Froelich, A., Tasarek, S. (2014). Application of gellan gum in pharmacy and
700 medicine. *International journal of pharmaceutics, 466*, 328-40.

Pasqui, E., De Cagna, M., Barbucci, R. (2012). Polysaccharide-based hydrogels: the key role of water in affecting mechanical properties. *Polymers*, *4*, 1517-34.

Payen S. (2007). *Integration of Hydrogels and Plastics Into Microfabrication Processes Towards a MEMS RF-Interrogated Biosensor*, University of California, Berkeley, ProQuest, (Chapter 3, p. 37).

Peyton, S.R., Putnam, A.J. (2005). Extracellular matrix rigidity governs smooth muscle cell motility in a biphasic fashion. *Journal of cellular physiology*, *204*, 198-209.

Pfeiffer, E., Vickers, S.M., Frank, E., Grodzinsky, A.J., Spector, M. (2008). The effects of glycosaminoglycan content on the compressive modulus of cartilage engineered in type II collagen scaffolds. *Osteoarthritis and Cartilage*, *16*, 1237-44.

Prajapati, V.D., Jani, G.K., Zala, B.S., Khutliwala, T.A. (2013). An insight into the emerging exopolysaccharide gellan gum as a novel polymer. *Carbohydrate polymers*, *93*, 670-8.

Santhanam, S., Liang, J., Struckhoff, J., Hamilton, P.D., Ravi, N. (2016). Biomimetic hydrogel with tunable mechanical properties for vitreous substitutes. *Acta Biomaterialia*, *43*, 327-37.

Shah, D., Maiti, P., Jiang, D.D., Batt, C.A., Giannelis, E.P. (2005). Effect of nanoparticle mobility on toughness of polymer nanocomposites. *Advanced Materials*, *17*, 525-8.

Shin, H., Olsen, B.D., Khademhosseini, A. (2014). Gellan gum microgel-reinforced cell-laden gelatin hydrogels. *Journal of Materials Chemistry B*, *2*, 2508-16.

Silva, N.A., Cooke, M.J., Tam, R.Y., Sousa, N., Salgado, A.J., Reis, R.L., Shoichet, M.S. (2012). The effects of peptide modified gellan gum and olfactory ensheathing glia cells on neural stem/progenitor cell fate. *Biomaterials*, *33*, 6345-54.

Smith, A.M., Shelton, R., Perrie, Y., Harris, J.J. (2007). An initial evaluation of gellan gum as a material for tissue engineering applications. *Journal of biomaterials applications*, *22*, 241-54.

Van Vlierberghe, S., Dubruel, P., Schacht, E. (2011). Biopolymer-based hydrogels as scaffolds for tissue engineering applications: a review. *Biomacromolecules*, *12*, 1387-408.

Vergaro, V., Abdullayev, E., Lvov, Y.M., Zeitoun, A., Cingolani, R., Rinaldi, R., Leporatti, S. (2010). Cytocompatibility and uptake of halloysite clay nanotubes. *Biomacromolecules*, *11*, 820-6.

Wagenseil, J.E., Wakatsuki, T., Okamoto, R.J., Zahalak, G.I., Elson, E.L. (2003). One-dimensional viscoelastic behavior of fibroblast populated collagen matrices. *Journal of biomechanical engineering*, *125*, 719-25.

Wang, C., Gong, Y., Lin, Y., Shen, J., Wang, D.A. (2008). A novel gellan gel-based microcarrier for anchorage-dependent cell delivery. *Acta Biomaterialia*, *4*, 1226-34.

White, R.D., Bavykin, D.V., Walsh, F.C. (2012). The stability of halloysite nanotubes in acidic and alkaline aqueous suspensions. *Nanotechnology*, *23*, *065705*, 1-10.

Yuan, P., Tan, D., Annabi-Bergaya, F. (2015). Properties and applications of halloysite nanotubes: recent research advances and future prospects. *Applied Clay Science*, *112*, 75-93.

Zhang, Y., Tang, A., Yang, H., Ouyang, J. (2016). Applications and interfaces of halloysite nanocomposites. *Applied Clay Science*, *119*, 8-17.

Zhao, X., Huebsch, N., Mooney, D.J., Suo, Z. (2010). Stress-relaxation behavior in gels with ionic and covalent crosslinks. *Journal of Applied Physics*, *107*, 063509-1.

Zhao, S., Shen, Z., Wang, J., Li, X., Zeng, Y., Wang, B., He, Y., Du, Y. (2014). Glycerol-mediated nanostructure modification leading to improved transparency of porous polymeric scaffolds for high performance 3D cell imaging. *Biomacromolecules*, *15*, 2521-31.

Zhou, W.Y., Guo, B., Liu, M., Liao, R., Rabie, A.B.M., Jia, D. (2010). Poly (vinyl alcohol)/halloysite nanotubes bionanocomposite films: properties and in vitro osteoblasts and fibroblasts response. *Journal of Biomedical Materials Research Part A*, *93*, 1574-87.